Search for muon-neutrino emission from GeV and TeV gamma-ray flaring blazars using five years of data of the ANTARES telescope

arXiv:1506.07354v1 [astro-ph.HE] 24 Jun 2015

S. Adrián-Martínez[1] A. Albert[2] M. André[3] G. Anton[4] M. Ardid[1]
J.-J. Aubert[5] B. Baret[6] J. Barrios-Martí[7] S. Basa[8] V. Bertin[5]
S. Biagi[18] C. Bogazzi[11] R. Bormuth[11,12] M. Bou-Cabo[1]
M.C. Bouwhuis[11] R. Bruijn[11,13] J. Brunner[5] J. Busto[5]
A. Capone[14,15] L. Caramete[16] J. Carr[5] T. Chiarusi[9] M. Circella[17]
R. Coniglione[18] H. Costantini[5] P. Coyle[5] A. Creusot[6]
I. Dekeyser[19] A. Deschamps[20] G. De Bonis[14,15] C. Distefano[18]
C. Donzaud[6,21] D. Dornic[5] D. Drouhin[2] A. Dumas[22] T. Eberl[4]
D. Elsässer[23] A. Enzenhöfer[4,5] K. Fehn[4] I. Felis[1] P. Fermani[14,15]
F. Folger[4] L.A. Fusco[9,10] S. Galatà[6] P. Gay[22] S. Geißelsöder[4]
K. Geyer[4] V. Giordano[24] A. Gleixner[4] R. Gracia-Ruiz[6] K. Graf[4]
H. van Haren[25] A.J. Heijboer[11] Y. Hello[20] J.J. Hernández-Rey[7]
A. Herrero[1] J. Hößl[4] J. Hofestädt[4] C. Hugon[26,27] C.W James[4]
M. de Jong[11,12] M. Kadler[23] O. Kalekin[4] U. Katz[4] D. Kießling[4]
P. Kooijman[11,28,13] A. Kouchner[6] I. Kreykenbohm[29]
V. Kulikovskiy[18,30] R. Lahmann[4] G. Lambard[7] D. Lattuada[18] D.
Lefèvre[19] E. Leonora[24] S. Loucatos[32] S. Mangano[7] M. Marcelin[8]
A. Margiotta[9,10] J.A. Martínez-Mora[1] S. Martini[19] A. Mathieu[5]
T. Michael[11] P. Migliozzi[33] A. Moussa[34] C. Mueller[23] M. Neff[4]
E. Nezri[8] G.E. Păvălaş[16] C. Pellegrino[9,10] C. Perrina[14,15]
P. Piattelli[18] V. Popa[16] T. Pradier[35] C. Racca[2] G. Riccobene[18]
R. Richter[4] K. Roensch[4] A. Rostovtsev[36] M. Saldaña[1] D. F.
E. Samtleben[11,12] M. Sanguineti[26,27] P. Sapienza[18] J. Schmid[4]
J. Schnabel[4] S. Schulte[11] F. Schüssler[32] T. Seitz[4] C. Sieger[4]
M. Spurio[9,10] J.J.M. Steijger[11] Th. Stolarczyk[32]
A. Sánchez-Losa[7] M. Taiuti[26,27] C. Tamburini[19] A. Trovato[18]
M. Tselengidou[4] C. Tönnis[7] D. Turpin[5] B. Vallage[32] C. Vallée[5]
V. Van Elewyck[6] E. Visser[11] D. Vivolo[33,37] S. Wagner[4]
J. Wilms[29] J.D. Zornoza[7] J. Zúñiga[7]

[1] Institut d'Investigació per a la Gestió Integrada de les Zones Costaneres (IGIC) - Universitat Politècnica de València. C/ Paranimf 1 , 46730 Gandia, Spain.

[2] GRPHE - Université de Haute Alsace - Institut universitaire de technologie de Colmar, 34 rue du Grillenbreit BP 50568 - 68008 Colmar, France

[3] Technical University of Catalonia, Laboratory of Applied Bioacoustics, Rambla Exposició,08800 Vilanova i la Geltrú,Barcelona, Spain

[4] Friedrich-Alexander-Universität Erlangen-Nürnberg, Erlangen Centre for Astroparticle Physics, Erwin-Rommel-Str. 1, 91058 Erlangen, Germany

[5] CPPM, Aix-Marseille Université, CNRS/IN2P3, Marseille, France

[6] APC, Université Paris Diderot, CNRS/IN2P3, CEA/IRFU, Observatoire de Paris, Sorbonne Paris Cité, 75205 Paris, France

[7] IFIC - Instituto de Física Corpuscular, Edificios Investigación de Paterna, CSIC - Universitat de València, Apdo. de Correos 22085, 46071 Valencia, Spain

[8] LAM - Laboratoire d'Astrophysique de Marseille, Pôle de l'Étoile Site de Château-Gombert, rue Frédéric Joliot-Curie 38, 13388 Marseille Cedex 13, France

[9] INFN - Sezione di Bologna, Viale Berti-Pichat 6/2, 40127 Bologna, Italy

[10] Dipartimento di Fisica e Astronomia dell'Università, Viale Berti Pichat 6/2, 40127 Bologna, Italy

[11] Nikhef, Science Park, Amsterdam, The Netherlands

[12] Huygens-Kamerlingh Onnes Laboratorium, Universiteit Leiden, The Netherlands

[13] Universiteit van Amsterdam, Instituut voor Hoge-Energie Fysica, Science Park 105, 1098 XG Amsterdam, The Netherlands

[14] INFN -Sezione di Roma, P.le Aldo Moro 2, 00185 Roma, Italy

[15] Dipartimento di Fisica dell'Università La Sapienza, P.le Aldo Moro 2, 00185 Roma, Italy

[16] Institute for Space Science, RO-077125 Bucharest, Măgurele, Romania

[17] INFN - Sezione di Bari, Via E. Orabona 4, 70126 Bari, Italy

[18] INFN - Laboratori Nazionali del Sud (LNS), Via S. Sofia 62, 95123 Catania, Italy

[19] Mediterranean Institute of Oceanography (MIO), Aix-Marseille University, 13288, Marseille, Cedex 9, France; UniversitÃĹ du Sud Toulon-Var, 83957, La Garde Cedex, France CNRS-INSU/IRD UM 110

[20] Géoazur, Université Nice Sophia-Antipolis, CNRS, IRD, Observatoire de la Côte d'Azur, Sophia Antipolis, France

[21] Univ. Paris-Sud , 91405 Orsay Cedex, France

[22] Laboratoire de Physique Corpusculaire, Clermont Univertsité, Université Blaise Pascal, CNRS/IN2P3, BP 10448, F-63000 Clermont-Ferrand, France

[23] Institut für Theoretische Physik und Astrophysik, Universität Würzburg, Emil-Fischer Str. 31, 97074 WÂÿrzburg, Germany

[24] INFN - Sezione di Catania, Viale Andrea Doria 6, 95125 Catania, Italy

[25] Royal Netherlands Institute for Sea Research (NIOZ), Landsdiep 4,1797 SZ 't Horntje (Texel), The Netherlands

[26] INFN - Sezione di Genova, Via Dodecaneso 33, 16146 Genova, Italy

[27] Dipartimento di Fisica dell'Università, Via Dodecaneso 33, 16146 Genova, Italy

[28] Universiteit Utrecht, Faculteit Betawetenschappen, Princetonplein 5, 3584 CC Utrecht, The Netherlands

[29] Dr. Remeis-Sternwarte and ECAP, Universität Erlangen-Nürnberg, Sternwartstr. 7, 96049 Bamberg, Germany

[30] Moscow State University,Skobeltsyn Institute of Nuclear Physics,Leninskie gory, 119991 Moscow, Russia

[31] Dipartimento di Fisica ed Astronomia dell'Università, Viale Andrea Doria 6, 95125 Catania, Italy

[32] Direction des Sciences de la Matière - Institut de recherche sur les lois fondamentales de l'Univers - Service de Physique des Particules, CEA Saclay, 91191 Gif-sur-Yvette Cedex, France

^{33}INFN -Sezione di Napoli, Via Cintia 80126 Napoli, Italy

^{34}University Mohammed I, Laboratory of Physics of Matter and Radiations, B.P.717, Oujda 6000, Morocco

^{35}IPHC-Institut Pluridisciplinaire Hubert Curien - Université de Strasbourg et CNRS/IN2P3 23 rue du Loess, BP 28, 67037 Strasbourg Cedex 2, France

^{36}ITEP - Institute for Theoretical and Experimental Physics, B. Cheremushkinskaya 25, 117218 Moscow, Russia

^{37}Dipartimento di Fisica dell'Università Federico II di Napoli, Via Cintia 80126, Napoli, Italy

E-mail: dornic@cppm.in2p3.fr, agustin.sanchez@ific.uv.es

Abstract. The ANTARES telescope is well-suited for detecting astrophysical transient neutrino sources as it can observe a full hemisphere of the sky at all times with a high duty cycle. The background due to atmospheric particles can be drastically reduced, and the point-source sensitivity improved, by selecting a narrow time window around possible neutrino production periods. Blazars, being radio-loud active galactic nuclei with their jets pointing almost directly towards the observer, are particularly attractive potential neutrino point sources, since they are among the most likely sources of the very high-energy cosmic rays. Neutrinos and gamma rays may be produced in hadronic interactions with the surrounding medium. Moreover, blazars generally show high time variability in their light curves at different wavelengths and on various time scales. This paper presents a time-dependent analysis applied to a selection of flaring gamma-ray blazars observed by the FERMI/LAT experiment and by TeV Cherenkov telescopes using five years of ANTARES data taken from 2008 to 2012. The results are compatible with fluctuations of the background. Upper limits on the neutrino fluence have been produced and compared to the measured gamma-ray spectral energy distribution.

Contents

1 Introduction

Neutrinos are unique messengers for studying the high-energy Universe as they are neutral, stable, interact weakly, and travel directly from their sources without absorption or deflection. Therefore, the reconstruction of the arrival directions of cosmic neutrinos would allow both the sources of the cosmic rays - supernova remnant shocks, active galactic nuclei jets, gamma-ray bursts, etc. [1] - and the relevant acceleration mechanisms acting within them to be identified.

The high-energy extragalactic sky is dominated by active galactic nuclei (AGN). Their spectral energy distribution can be described by two components: a low-energy one from radio to X-rays and a high-energy one from X-rays to very high-energy gamma rays. The low-energy component is generally attributed to synchrotron radiation in the relativistic jet by a non-thermal population of accelerated electrons and positrons; the origin of the second component is still under discussion. In leptonic models [2], it is ascribed to an inverse Compton process between the electrons and a low-energy photon field (their own synchrotron radiation, or external photons), while in hadronic models it originates from synchrotron emission by protons and secondary particles coming from p-γ or p-p interactions [3, 4]. Associated with these very high-energy gamma rays from π^0 decays, the decay of the charged pions gives rise to a correlated neutrino emission.

Flat-spectrum radio quasars (FSRQs) and BL Lacs, together classified as blazars, exhibit relativistic jets pointing almost directly towards the Earth, and are among the most violent variable high-energy phenomena in the Universe [5]. Blazars are particularly attractive potential neutrino sources, since they are among the most likely sources of the very high-energy cosmic rays [6, 7]. Several theoretical models predict high-energy neutrino emission from blazars that yield different shapes and normalisations for the expected energy spectrum [8–11]. In addition, the models also suffer from large uncertainties that originate, for instance, from unknowns in the model parameters, the luminosity functions and the source evolution. For example, the FSRQs are predicted to be more promising neutrino candidates than BL Lacs in Ref. [12], while in Ref. [13] the opposite is predicted. Several authors even estimate more optimistic spectra with spectral indexes up to one [14, 15]. The E^{-2} spectrum, generally

expected from Fermi acceleration of cosmic rays in astrophysical sources, is used as a reference spectrum. An energy cutoff seems to be present in most sources observed in gamma rays [16]. For these reasons, to cover the majority of the range allowed by the models accessible to the ANTARES sensitivity (see Section 2), four neutrino-energy spectra are tested in this analysis: E^{-2}, $E^{-2} \exp(-E/10 \text{ TeV})$, $E^{-2} \exp(-E/1 \text{ TeV})$ and E^{-1}, where E is the neutrino energy.

In the ANTARES telescope [17], events are primarily detected underwater by observing the Cherenkov light induced by relativistic muons in the darkness of the deep sea. Owing to their low interaction probablility, only neutrinos have the ability to cross the Earth. Therefore, an upgoing muon is an unambiguous signature of a neutrino interaction close to the detector. The detection of cosmic neutrinos with neutrino telescopes is very challenging because of the small neutrino interaction cross-section and the high background of atmospheric neutrinos from cosmic-ray interactions in the atmosphere. To distinguish astrophysical neutrino events from background events (muons and neutrinos) generated in the atmosphere, energy and direction reconstructions have been used in several searches [18–20]. To improve the signal-to-noise discrimination, the arrival time information can be used, significantly reducing the effective background [21, 22]. Blazars are known to show time variability at different wavelengths and on various time scales [23–25]. The associated neutrino emission may exhibit similar variability, and this is used in time-dependent methods to improve the detection probability with respect to time-integrated approaches.

In this paper, the results of a time-dependent search for cosmic neutrino sources using the ANTARES data taken from 2008 to 2012 is presented. This extends a previous ANTARES analysis [26] where only the last four months of 2008 were considered. The analysis is applied to a list of promising blazar candidates detected in GeV gamma rays by the LAT instrument onboard the FERMI satellite, and to a list of blazar flares reported by TeV gamma-ray experiments (H.E.S.S., MAGIC and VERITAS). After a brief description of the apparatus, the data selection and the detector performances are presented in Section 2. The point-source search algorithm used in this time-dependent analysis is explained in Section 3. The results of the GeV and TeV flare searches are presented in Sections 4 and 5, respectively, and discussed in Section 6.

2   The ANTARES neutrino telescope

The ANTARES collaboration completed the construction of a neutrino telescope in the Mediterranean Sea with the connection of its twelfth detector line in May 2008 [17]. The telescope is located 40 km off the Southern coast of France (42°48'N, 6°10'E), at a depth of 2475 m. It comprises a three-dimensional array of 10" photomultipliers [27], each housed in a glass sphere (Optical Modules, OMs [28]), distributed along twelve slender lines anchored at the sea bottom and kept taut by a buoy at the top. The lines are connected to a central junction box, which in turn is connected to shore via an electro-optical cable. Since lines are subject to the sea current and can change shape and orientation, a positioning system comprising hydrophones, compasses and tiltmeters is used to monitor the detector geometry [29]. The main goal of the experiment is to search for neutrinos of astrophysical origin by detecting high-energy muons (>100 GeV) created by neutrino charged-current interactions in the vicinity of the detector.

The arrival time and intensity of the Cherenkov light on the OMs are digitised into 'hits' and transmitted to shore, where events containing muons are separated from the optical backgrounds due to natural radioactive decays and bioluminescence, and stored on disk. A

detailed description of the detector and of the data acquisition is given in Ref. [17, 30]. The data used in this analysis were taken with the full detector during the period from September 6th, 2008 up to December 31st, 2012 (54720-56292 modified Julian day). Filters are applied in order to exclude periods in which the bioluminescence-induced optical background was high. The resulting effective livetime is 1044 days.

Atmospheric neutrinos are the main source of background in the search for astrophysical neutrinos. These neutrinos are produced from the interaction of cosmic rays in the Earth's atmosphere. To account for this background, muon neutrino events are simulated using the GENHEN package [31] according to the parametrisation of the atmospheric neutrino flux from Ref. [32]. An additional source of background is due to mis-reconstructed atmospheric muons. Downgoing atmospheric muons are simulated with the program MUPAGE [33, 34] which provides muon bundles at the detector. The full Monte Carlo chain, which includes the simulation of Cherenkov photon production and of the detector response, is described in Ref. [35].

The applied track reconstruction algorithm is the same as that used in the standard ANTARES point-source search [19]. This algorithm derives the muon track parameters that maximise a likelihood function built from the difference between the expected and the measured arrival times of the hits from the Cherenkov photons emitted along the muon track. This maximisation takes into account the Cherenkov photons that scatter in the water and the additional photons that are generated by secondary particles (e.g. electromagnetic showers created along the muon trajectory).

The muon track reconstruction returns two quality parameters, namely the track-fit quality parameter, Λ, and the estimated angular uncertainty on the fitted muon track direction, β. Cuts on these parameters are used to improve the signal-to-noise ratio. To ensure a good directional reconstruction of the selected neutrino candidates, $\beta < 1°$ is required. Figure 1 shows the distribution of the error estimate β. This cut rejects 47% of the atmospheric muons which are mis-reconstructed as upgoing tracks. After quality cuts, all events with a zenith angle $\cos(\theta) > -0.15$ are selected. Compared to a strict upgoing event selection, this cut provides a gain in visibility of on average 15% for all sources with a declination above -20°. Figure 2 shows the distribution of the reconstructed cosine of the zenith angle for both data and simulation. The value of the cut on Λ is optimised for each source on the basis of maximising a model discovery potential [22] for a 3σ significance level for each neutrino spectrum. The distribution of Λ for events selected after applying the β and $\cos(\theta)$ cuts is shown in Figure 3. The optimum Λ values range from -5.5 to -5.0 depending on the source and the background characteristics during the flares.

The energy of each events is estimated by exploiting the correlation between the energy deposition, dE/dX, and the primary energy [36, 37]. The systematic uncertainty in the dE/dX energy estimator is 10%. This is accounted for by smearing the simulated signal values by a gaussian function with this RMS value.

The pointing accuracy has been determined directly from the data using the moon shadow [38] and is of the order of 0.63° (C.L. 90%). Figure 4 shows the cumulative distribution of the angular difference between the reconstructed muon direction and the neutrino direction with an assumed spectrum proportional to E^{-2}, $E^{-2}\exp(-E/10 \text{ TeV})$, $E^{-2}\exp(-E/1 \text{ TeV})$ and E^{-1}. For example, the median resolution is estimated to be 0.43±0.1° for the reference E^{-2} energy spectrum.

The acceptance (with units of GeV cm^2 s^1) is the proportionality factor between a given energy flux and the corresponding number of signal events expected in the detector
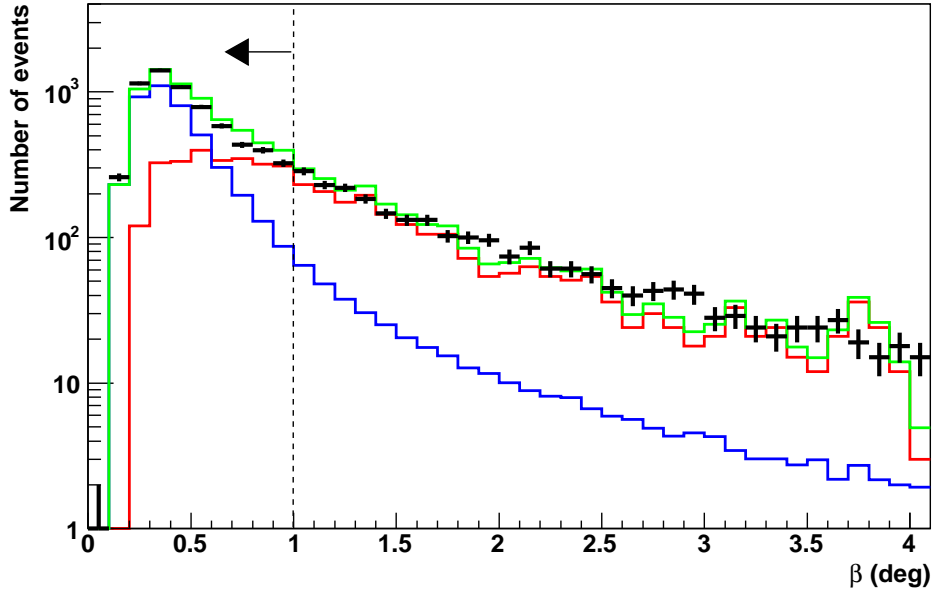
Figure 1. Distribution of the estimated error on the direction of the reconstructed muon track after applying a zenith angle cut $\cos(\theta) > -0.15$ and a cut on the quality variable $\Lambda > -5.3$. The blue line shows the simulated upgoing atmospheric neutrinos, the red line the mis-reconstructed atmospheric muons, the green line the sum of both contributions, and the black crosses the data. The vertical dashed line with the arrow shows where the selection cut is applied ($\beta < 1°$).

after selection. Thus, a certain neutrino spectrum has to be assumed. For example, for $\Lambda > -5.3$, the acceptances as a function of the source declination are shown for each considered spectra in Figure 5. For the limit setting, a 15% systematic uncertainty on the acceptance is considered [19].

3 Time-dependent search method

The time-dependent point-source analysis is performed using an unbinned method based on a likelihood-ratio maximisation. The data are parameterised as a two-component mixture of signal and background. The signal is expected to be small so that the full data sample (N events) can be treated as background. The expected number of events are $\mathcal{N}_{\mathrm{S}}$ (unknown) and $\mathcal{N}_{\mathrm{B}}$ (known) and the probabilities for signal and background for an event i, at time t_i, energy estimate dE/dX_i, declination δ_i and Ψ_i are $\mathcal{S}_i$ and $\mathcal{B}_i$ respectively. $\mathcal{S}$ and $\mathcal{B}$ respectively. The probability $\mathcal{P}$ and the likelihood $\mathcal{L}$ are:

$$\mathcal{P}_i = \mathcal{N}_{\mathrm{S}}\mathcal{S}_i + \mathcal{N}_{\mathrm{B}}\mathcal{B}_i \tag{3.1}$$

$$\ln \mathcal{L} = \left(\sum_{i=1}^{N} \ln[\mathcal{N}_{\mathrm{S}}\mathcal{S}_i + \mathcal{N}_{\mathrm{B}}\mathcal{B}_i] \right) - [\mathcal{N}_{\mathrm{S}} + \mathcal{N}_{\mathrm{B}}] \tag{3.2}$$

To discriminate the signal-like events from the background ones, these probabilities are described by the product of three components related to the direction, energy, and timing of each event. For an event i, the signal probability is:
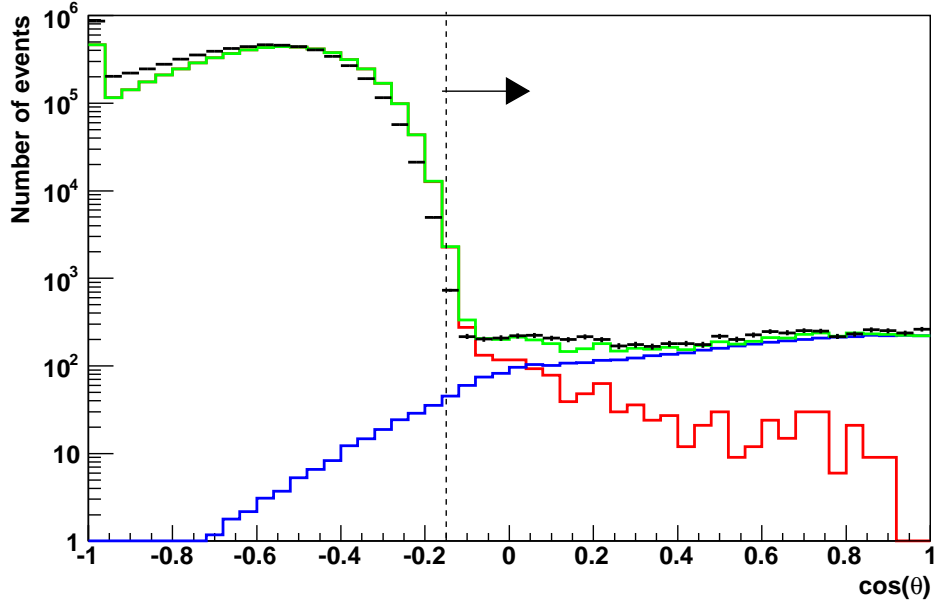
Figure 2. Distribution of the reconstructed cosine of the zenith angle of the events (black crosses) with $\beta < 1°$ and $\Lambda > $ -5.3. The simulated distributions are shown for atmospheric muons (red) and upgoing neutrinos (blue) and the green line is the sum of both components. The vertical dashed line with the arrow shows where the cut on the zenith angle is applied in order to select mainly upgoing events (those with larger zenith angles).

$$S_i = \mathcal{S}^{\text{space}}(\Psi_i(\alpha_s, \delta_s)) \cdot \mathcal{S}^{\text{energy}}(dE/dX_i) \cdot \mathcal{S}^{\text{time}}(t_i + lag) \qquad (3.3)$$

where $\mathcal{S}^{\text{space}}$ is a parameterisation of the point spread function, i.e., $\mathcal{S}^{\text{space}}(\Psi_i(\alpha_s, \delta_s))$ the probability to reconstruct an event i at an angular distance Ψ_i from the true source location (α_s, δ_s). The energy PDF $\mathcal{S}^{\text{energy}}$ is parametrised with the normalised distribution of the muon energy estimator of an event according to the studied energy spectrum. Figure 6 illustrates the energy PDF of these four tested energy spectra. For the generation of signal events, the correlation between the angular error and the energy of the muon track is taken into account. The shape of the time PDF, $\mathcal{S}^{\text{time}}$, for the signal event is extracted directly from the gamma-ray light curve assuming the proportionality between the gamma-ray and the neutrino fluxes. A possible lag of up to ± 5 days has been introduced in the likelihood to allow for small lags in the proportionality. This corresponds to a possible shift of the entire time PDF. The lag parameter is fitted in the likelihood maximisation together with the number of fitted signal events in the data.

The background probability for an event i is:

$$\mathcal{B}_i = \mathcal{B}^{\text{space}}(\delta_i) \cdot \mathcal{B}^{\text{energy}}(dE/dX_i) \cdot \mathcal{B}^{\text{time}}(t_i) \qquad (3.4)$$

The directional PDF B^{space}, the energy PDF B^{energy} and the time PDF B^{time} for the background are derived from data using, respectively, the observed declination distribution of selected events in the sample, the measured distribution of the energy estimator, and the observed time distribution of all the reconstructed muons. Figure 7 shows the time distribution
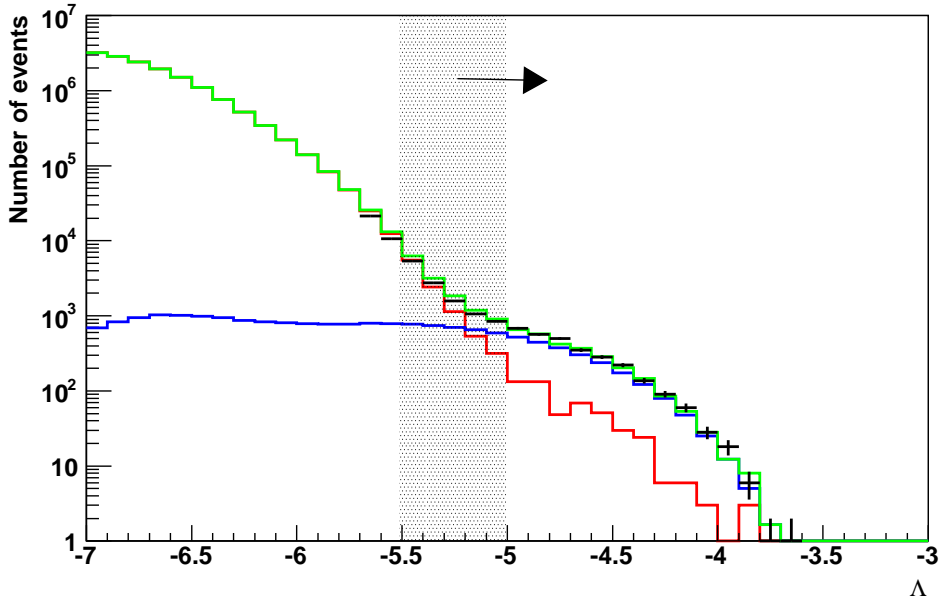
Figure 3. Distribution of the reconstruction quality variable Λ for tracks (black crosses) which have an angular uncertainty estimate $\beta < 1°$ and zenith angle $\cos(\theta) > $ -0.15. The simulated distributions are shown for atmospheric muons (red) and upgoing neutrinos (blue) and the green line is the sum of both components. The vertical dashed area with the arrow shows where the optimised selection cuts stand for the various tested sources.

of all reconstructed events, including both downgoing and selected events. Once normalised, the first downgoing distribution is used directly as the time PDF for the background. Null values indicate the absence of data taken during these periods (e.g. detector in maintenance) or data with a very poor quality (high bioluminescence).

The goal of the unbinned search is to determine, in a given direction in the sky and at a given time, the relative contribution of each component, and to calculate the probability to have a signal above a given background model. This is done via the test statistic, λ, defined as the ratio of the probability for the hypothesis of background and signal ($H_{\text{sig+bkg}}$) over the probability of only background (H_{bkg}):

$$\lambda = \sum_{i=1}^{N} \ln \frac{\mathcal{P}(x_i|H_{\text{sig+bkg}}(\mathcal{N}_{\text{S}}))}{\mathcal{P}(x_i|H_{\text{bkg}})} \tag{3.5}$$

where $\mathcal{N}_{\text{S}}$ and N are respectively the unknown number of signal events and the total number of events in the considered data sample, and x_i are the observed event properties (δ_i, RA_i, dE/dX_i and t_i)

The evaluation of the test statistic is performed by generating pseudo-experiments simulating background and signal in a 30° cone around the considered source according to the background-only and background plus signal hypotheses. The direction of the background events are generated by randomly sampling the declination distribution from the background probablility $\mathcal{B}$ and the right ascension from a uniform distribution. Signal events are simulated by first sampling the time and the energy of the simulated events by randomly generating from B^{time} and B^{energy}, respectively. Then, the angular distance from the coordinates of the
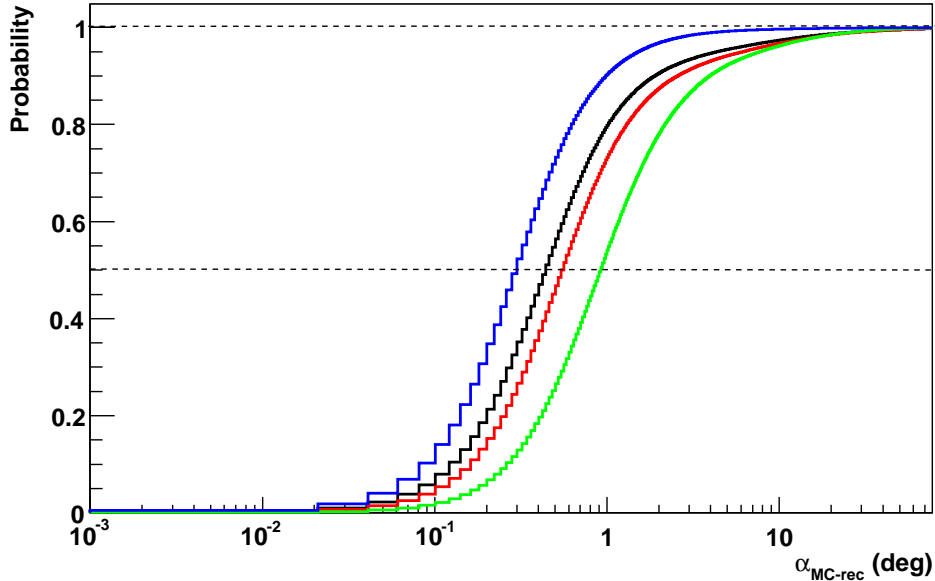
Figure 4. Cumulative distribution of the angle, α, between the true Monte Carlo neutrino direction and the reconstructed muon direction for neutrino events selected for this analysis with E^{-2} (black line, with median 0.43°), $E^{-2}\exp(-E/10\text{ TeV})$ (red line, with median 0.55°), $E^{-2}\exp(-E/1\text{ TeV})$ (green line, with median 0.90°) and E^{-1} (blue line, with median 0.29°).

studied source $\Psi_i(\alpha_s, \delta_s)$ is sampled as a function of the declination and of the estimated energy.

The null hypothesis is given by $\mathcal{N}_S = 0$ (λ_0) (i.e. the background-only hypothesis H_{bkg}). The obtained value of λ for the data, λ_{data}, is then compared to the distribution of λ_0 obtained by pseudo-experiments. Large values of λ_{data} compared to the distribution of λ_0 reject the null hypothesis with a confidence level depending on the fraction of the λ_0 distribution above λ_{data}. This fraction of trials above λ_{data} is referred to as the p-value. The discovery potential is then defined as the average number of signal events required to achieve a p-value lower than $2.7\ 10^{-3}$ ($5.7\ 10^{-7}$) $(3(5)\sigma)$ in 50% of the trials.

The performance of the time-dependent analysis is computed with a toy experiment with a source assuming a square-shaped flare with a width varying from 1 to 2000 days assuming a flat background period of 2000 days. Figure 8 shows the average number of events required for a 5σ discovery for a single source located at a declination of -40° and following an E^{-2} energy spectrum, as a function of the total width of the flare periods. These numbers are compared to those obtained without the selection of time intervals corresponding to flaring periods. For time ranges characteristic of flaring activity, the time-dependent search presented here improves the discovery potential by on-average a factor 2-3 with respect to a standard time-integrated point-source search [19] under the assumption that the neutrino emission is correlated with the gamma-ray flaring activity.
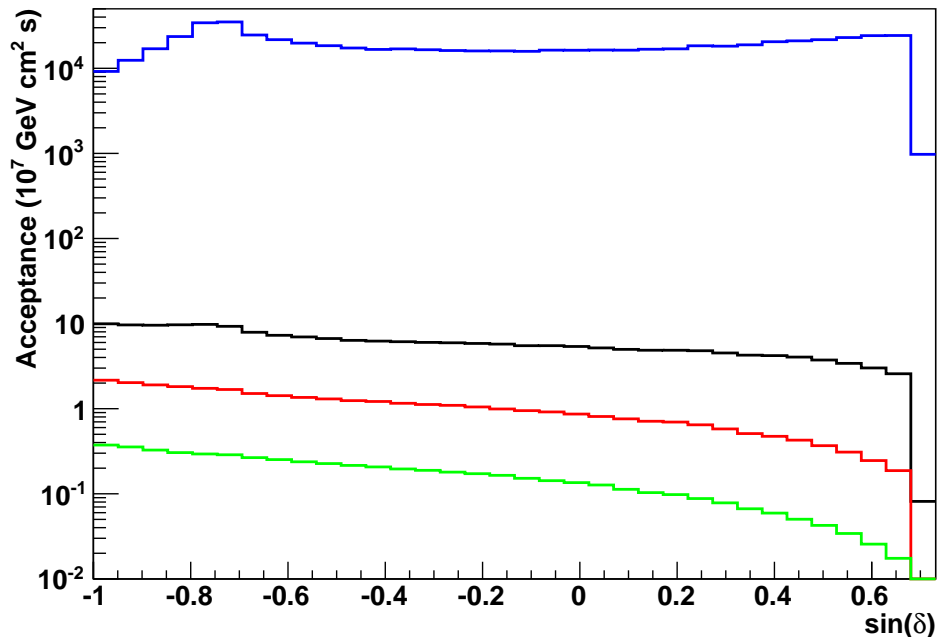
Figure 5. Acceptance of the analysis as a function of the sine of the declination for E^{-2} (black), $E^{-2} \exp(-E/10 \text{ TeV})$ (red), $E^{-2} \exp(-E/1 \text{ TeV})$ (green) and E^{-1} (blue) neutrino energy spectra. The events are selected with $\beta < 1^o$, $\cos(\theta) > $ -0.15 and $\Lambda > $ -5.3. The different shape between the acceptance for E^{-1} and the rest of the neutrino spectra is due to the Earth absorption for very high-energy events.

4 Search for neutrino emission from gamma-ray flares detected by FERMI

The time-dependent analysis described in the previous section is applied to bright and variable Fermi blazar sources reported in the second Fermi LAT catalogue [39] and in the LBAS catalogue (LAT Bright AGN sample [16]). The sources located in the part of the sky visible to ANTARES ($\delta < 35°$) with a flux greater than 10^{-9} photons $\cdot$ cm^{-2} $\cdot$ s^{-1} above 1 GeV, a test statistic $TS > 25$ (corresponding to a detection significance of more than 4 sigma) and a significant time variability are selected. This list is completed by adding sources reported as flaring in the Fermi Flare Advocates in 2011 and 2012 [40]. The final list includes a total of 153 sources.

Light curves for the selected sources are produced using the Fermi Public Release Pass 7 data using the source class event selection (evclass=2) and the Fermi Science Tools v9r35p1 package [41]. Following the standard event selection cuts proposed by the Fermi-LAT Collaboration [42], the data are filtered using the *gtselect* tool to select only events which are most likely gamma-rays. Light curves are computed from the photon counting data in a cone of two-degree radius around each source direction, corrected by the total exposure. With this method the diffuse background contributions are not subtracted. This limits the validity of this method to only bright gamma-ray sources, but does not affect the flare identification in these sources. Therefore, sources which are close to the galactic plane (galactic latitude $< 10°$) or have others sources within a two-degree cone (or 3° for very bright sources) are excluded. The baseline is then removed for the time PDF definition. The resulting light
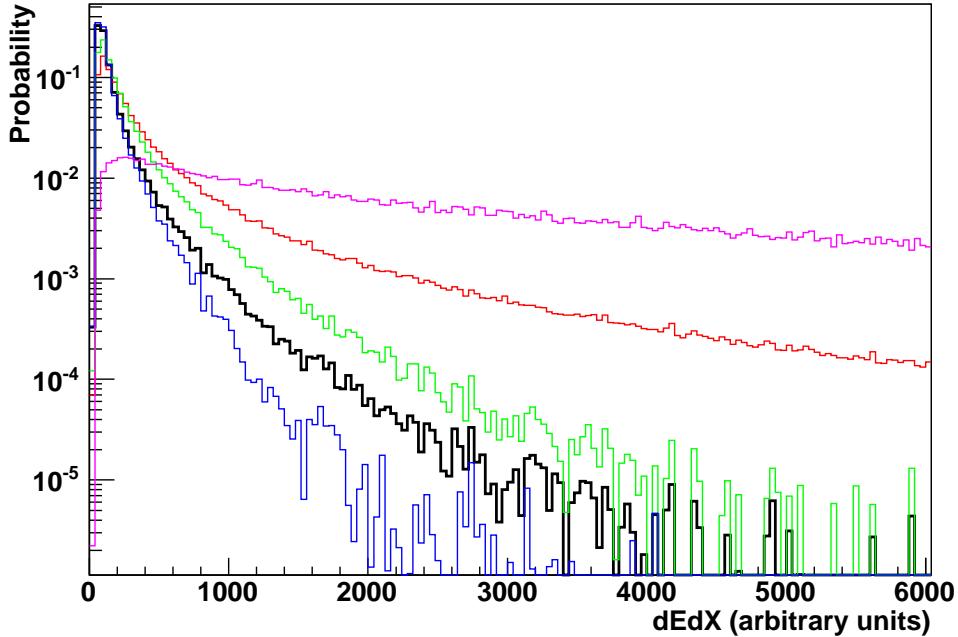
Figure 6. Distribution of the energy PDF of the background events (black) and of the signal events assuming an energy spectrum following E^{-2} (red), $E^{-2} \exp(-E/10 \text{ TeV})$ (green), $E^{-2} \exp(-E/1 \text{ TeV})$ (blue) and E^{-1} (purple). Each distribution is normalised to unity.

curves correspond to the one-day-binned time evolution of the average gamma-ray flux above a threshold of 100 MeV from August 2008 to December 2012. This method has the main advantage of producing continuous and complete gamma-ray light curves. Figure 9 (a) shows the resulting light curve for the source 3C273. This aperture photometry method agrees with the results of the likelihood analysis (an alternative method used for the LAT data analysis). The exposure is calculated using the *gtexposure* tool, which is also part of the Fermi framework.

A maximum likelihood block (MLB) algorithm [43–45] is used to remove noise from the light curves by iterating over the data points and selecting periods during which data are consistent with a constant flux within statistical errors. The description of the light curve in terms of N_B periods of constant emission is obtained with the following likelihood:

$$\ln L = \sum_{n_B \in N_B} \frac{\left(\sum_{i \in n_B} \frac{x_i}{\sigma_i^2} \right)^2}{\sum_{i \in n_B} \frac{1}{\sigma_i^2}} \qquad (4.1)$$

where x_i is the flux measurement of the data point i and σ_i is the error of the flux measurement i. Since this likelihood would maximise when there are as many periods as data points, while only a few periods are required to describe the light curve, the following prior $\mathcal{P}$ is added to the likelihood:

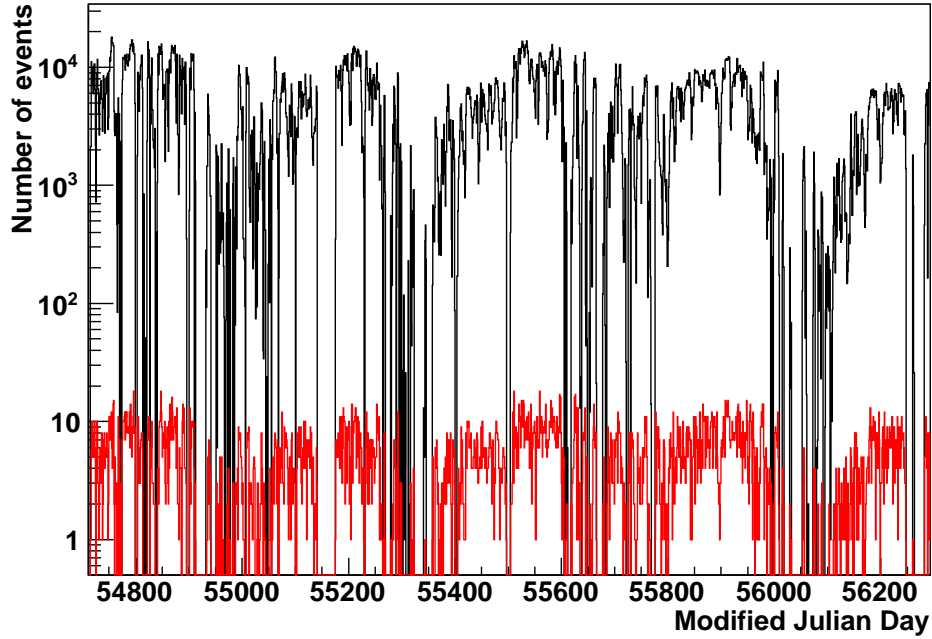$$\ln \mathcal{P} = -N_B \ln \mathcal{N}$$

Figure 7. Time distribution of the reconstructed events. Upper histogram (black): distribution of well-reconstructed events (including downgoing muons). Bottom histogram (red): distribution of the events selected by this analysis.
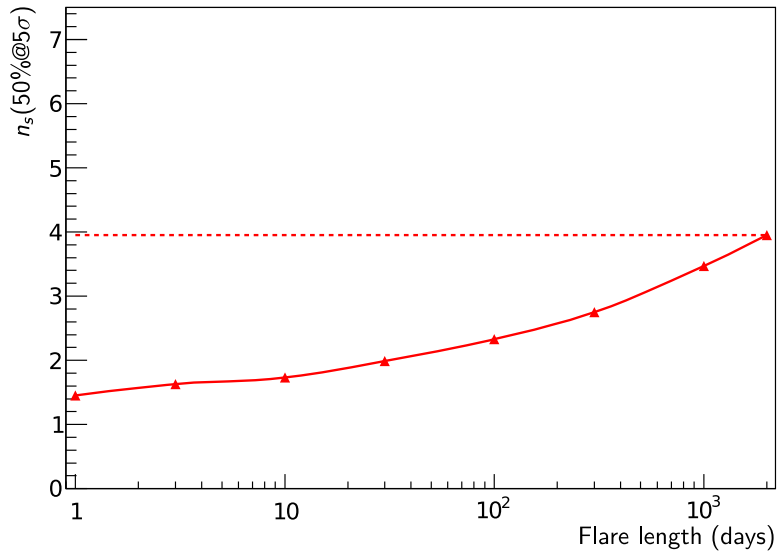

Figure 8. Average number of events required for a 5σ discovery (50% probability) for a source located at a declination of -40° and following an E^{-2} energy spectrum as a function of the total width of the flaring periods (solid line). These numbers are compared to those obtained without using the timing information (dashed line).

where $\mathcal{N}$ is the number of data points in the light curve. The algorithm searches in each iteration for the best two flux changes in the emission in each period already found and keeps them for the next iteration. The Figure 9 (b) shows the optimisation of the likelihood in the case of 3C273.

High-state periods are defined using a simple and robust method. The value of the steady state (i.e. baseline, BL) and its fluctuation (σ_{BL}) are determined with a Gaussian fit of the lower part of the distribution of the flux data points (Figure 9 (c)). The flaring periods are defined in three main steps. Firstly, seeds are identified by searching for points with an amplitude, or blocks with a fluence above $BL + 5\sigma_{BL}$. Then, each period is extended forward and backward up to an emission compatible with $BL + 1\sigma_{BL}$. An additional delay of 0.5 days is added before and after the flare in order to take into account that the precise time of the flare is not known (one-day binned light curve). Finally, spurious flares are discarded by requiring that each flare is visible in the three light curves produced with a gamma-ray threshold of 100, 300 and 1000 MeV. Figure 9 (d) shows an example of one flare of 3C273. With the above definition, a flare has a width of at least two days. Under the hypothesis that the neutrino emission follows the gamma-ray emission, the signal time PDF is the normalised de-noised light curve with only the high state periods (the other periods are set to zero). The final list includes 41 bright and variable Fermi blazars: 33 FSRQs, 7 BL Lacs and 1 unknown identification. Figure 10 shows the position of the selected Fermi Blazars together with the ANTARES visibility. The main characteristics of these blazars are reported in Table 1.

The results of the search is summarised in Table 2. Only three sources, 3C279, PKS10235-618 and PKS1124-186, have a pre-trial p-value lower than 10%. The lowest p-value, 3.3%, is obtained for 3C279 where one event is coincident with a large gamma-ray flare detected by Fermi/LAT in November 2008. Figure 11 shows the Fermi gamma-ray light curve of 3C279 with the time of the neutrino events, the estimated energy distribution, and the angular distribution of the events around the position of this source. This coincident event is reconstructed with 89 hits (energy deposition $dE/dX = 244$ in arbitrary units) distributed on ten lines with a track fit quality $\Lambda = -4.4$. The particle track direction is reconstructed at $0.3°$ from the source location. This event has already been reported in the previous analysis [26]. The post-trial probability, computed by taking into account the 41 searches, is 67%, and is thus compatible with background fluctuations.

In the absence of a discovery, upper limits on the neutrino fluence, $\mathcal{F}_\nu$, at 90% confidence level are computed using 5-95% of the energy range as:

$$\mathcal{F}_\nu = \Delta t \int_{E_{\min}}^{E_{\max}} dE \cdot E \frac{dN}{dE}$$

The emission duration, Δt, is computed using the time PDF and the effective livetime. The limits include the systematic errors and are calculated according to the classical (frequentist) method for upper limits [46]. Figure 12 gives these upper limits. IceCube has performed a similar time-dependent analysis [47] using data from 2008 to 2012, with 19 sources in common with the list presented in Table 1. For sources in the Southern Hemisphere, the limits computed by IceCube are of the same order of magnitude as the ANTARES limits while they are a factor 10 stronger for the sources in the Northen hemisphere thanks to IceCube's larger detector volume.

Table 1. List of bright variable Fermi blazars with significant flares selected for this analysis.

Name	OFGL name	Class	RA [°]	Dec [°]	Redshift
3C 454.3	J2254.0+1609	FSRQ	343.50	16.15	0.859
4C +21.35	J1224.9+2122	FSRQ	186.23	21.38	0.434
PKS 1510-08	J1512.7-0905	FSRQ	228.18	-9.09	0.360
3C 279	J1256.1-0548	FSRQ	194.03	-5.8	0.536
PKS 1502+106	J1504.3+1029	FSRQ	226.10	10.49	1.839
PKS 2326-502	J2329.2-4956	FSRQ	352.32	-49.94	0.518
3C 273	J1229.1+0202	FSRQ	187.28	2.05	0.158
AO 0235+164	J0238.6+1636	BLLac	39.65	16.61	0.940
PKS 0426-380	J0428.6-3756	FSRQ	67.17	-37.93	1.110
4C +28.07	J0334.3-3728	FSRQ	53.58	-37.47	1.206
PKS 0454-234	J0457.1-2325	FSRQ	74.28	-23.43	1.003
PKS 1329-049	J1332.0-0508	FSRQ	203.01	-5.14	2.150
PKS 0537-441	J0538.8-4405	BLLac	84.71	-44.08	0.896
4C +14.23	J0725.3+1426	FSRQ	111.33	14.44	1.038
PMNJ 0531-4827	J0532.0-4826	UNID	83.01	-48.44	/
PKS 0402-362	J0403.9-3604	BLLac	60.99	-36.07	1.417
PKS 1124-186	J1126.6-1856	FSRQ	171.66	-18.95	1.048
Ton 599	J1159.5+2914	FSRQ	179.88	29.25	0.725
PKS 2142-75	J2147.4-7534	FSRQ	326.87	-75.58	1.139
PKS 0208-512	J0210.8-5100	FSRQ	32.70	-51.2	1.003
PKS 0235-618	J0237.1-6136	FSRQ	39.29	-61.62	0.467
PKS 1830-211	J1833.6-2104	FSRQ	278.41	-21.08	2,507
PKS 2023-07	J2025.6-0736	FSRQ	306.42	-7.61	1.388
PKSB 1424-418	LJ1428.0-4206	FSRQ	217.01	-42.10	1.522
PMNJ 2345-1555	J2345.0-1553	FSRQ	356.27	-15.89	0.621
OJ 287	J0855.4+2009	BLLac	133.85	20.09	0.306
PKS 0440-00	J0442.7-0017	FSRQ	70.69	-0.29	0.845
PKS 0250-225	J0252.7-2218	FSRQ	43.20	-22.31	1.419
B22308+34	J2311.0+3425	FSRQ	347.77	34.43	1.187
B21520+31	J1522.1+3144	FSRQ	230.54	31.74	1.487
PKS 1730-13	J1733.1-1307	FSRQ	263.28	-13.13	0.902
PKS0244-470	J0245.9-4652	FSRQ	41.06	-47.06	1.385
PKS 0301-243	J0303.4-2407	BLLac	45.87	-24.13	0.26
CTA 102	J2232.4+1143	FSRQ	338.12	11.72	1.037
OG 050	J0532.7+0733	FSRQ	83.19	7.56	1.254
PMNJ 2331-2148	J2330.9-2144	FSRQ	352.75	-21.74	0.563
PKS0805-07	J0808-0751	BLLac	122.06	-7.85	1.837
PKS 2320-035	J2323.6-0316	FSRQ	350.91	-3.28	1.411
PKS 2227-08	J2229.7-0832	FSRQ	337.44	-8.55	1.560
OJ248	J0830.5+2407	FSRQ	127.72	24.18	0.942
PKS 2233-148	J2236.5-1431	BLLac	339.13	-14.53	0.325

Table 2. Results of the search for neutrinos in coincidence with Fermi blazar flares (three first rows) and TeV flares (last row). The total duration of all identified flares Δt, the optimised Λ_{opt} cuts, the number of required events for a 3σ discovery ($N_{3\sigma}$), the number of fitted signal events by the likelihood (N_{fit}), the fitted time lag (Lag) and the corresponding pre-trial (post-trial) probability are given together with the energy spectra.

Source	Δt	Λ_{opt}	$N_{3\sigma}$	N_{fit}	Lag	P-value	Post-trial	Spectrum
3C279	279 d	-5.3	2.5	0.8	-4 d	0.033	0.67	E^{-2}
PKS1124-186	73 d	-5.4	3.1	0.7	+4 d	0.059	0.94	$E^{-2}\exp(-E/1\mathrm{TeV})$
PKS0235-618	25 d	-5.7	1.5	0.6	-4 d	0.045	0.91	$E^{-2}\exp(-E/10\mathrm{TeV})$
PKS0447-439	10 d	-5.4	0.75	0.1	+5 d	0.10	0.55	$E^{-2}\exp(-E/1\mathrm{TeV})$

5 Search for neutrino emission from gamma-ray flares detected by TeV telescopes

Ground-based observatories such as H.E.S.S., MAGIC and VERITAS cannot monitor sources continuously, because they generally have a reduced field of view and a low duty cycle (e.g. only moonless nights). Nevertheless, these telescopes detect photons with energies from a few hundred GeV to a few TeV that may be better correlated with the neutrinos to which ANTARES is sensitive. These observatories often emit alerts reporting flares to Astronomer's Telegram or directly in a dedicated paper. When the start and stop times of the flare are known, the time PDF is assumed to be a single square-shaped flare with a minimum width of one day. Often, the beginning and the end of the flaring activity cannot be constrained accurately. In this case, a simple time cut is used, taking a time window including two days before and after the identified flare. Table 3 presents the list of seven TeV flares, their characteristics, and the publications from where this information is extracted. The flares are chosen for this analysis according to the same visibility criteria as for Fermi/LAT observations. The same analysis as described previously is performed assuming the same four energy spectra.

Six of the seven flares tested show no excess of events in the vicinity of the corresponding sources in the selected time windows. Only the blazar PKS0447-439 shows a pre-trial p-value lower than 10% in the case of the assumed $E^{-2}\exp(-E/1\,\mathrm{TeV})$ energy spectrum (cf Table 2). The corresponding post trial p-value is 55%, and is also consistent with background fluctuations. In the absence of a signal, upper limits on the neutrino fluence at 90% confidence level are computed including the systematic errors (Figure 13).

Table 3. List of TeV flares reported by the three telescopes H.E.S.S., MAGIC and VERITAS in the 2008-2012 period.

Name	Telescope	RA	Dec	Flaring days (MJD)	Reference
4C+21.35	MAGIC	186.2	21.4	55364-5	arXiv:1101.4645
PG 1553+113	MAGIC	239.0	11.2	55980-91 56037-8	arXiv:1109.5860
PKS 1424+240	MAGIC	216.8	23.8	54940-60	arXiv:1109.5860
1ES 1218+30.4	VERITAS	185.4	30.2	54860-5	arXiv:1005.3747
1ES 0229+200	VERITAS	38.2	20.3	55118-31	arXiv:1307.8091
J1943+213	H.E.S.S.	296.0	21.3	55040-60	arXiv:1103.0763
PKS0447-439	H.E.S.S.	72.4	-43.8	55174-84	arXiv:1303.1628

6 Discussion

Hadronic interactions predict neutrino emission in the TeV-PeV range associated with a flux of gamma rays. The prediction that the total neutrino energy flux F_ν is approximately equal to the total high-energy photon flux F_γ is relatively robust, at least when attributing this emission to a 100% hadronic origin [48, 49]. As it is not affected by pair production losses, the neutrino emission is expected to have energies systematically higher than the electromagnetic component. The Fermi measurement of the source flux in the 0.1-100 GeV range is an underestimate of the overall electromagnetic spectrum, since it covers only three decades of energy. This underestimates, around a factor of 2-3 [50], has to be taken into account in the comparison between neutrinos and gamma-rays. Moreover, the lack of TeV observations makes a direct comparison at the >TeV range difficult, and necessitates an extrapolation of the LAT data over several orders of magnitude. This extrapolation is performed using a fit of the Fermi data with a log-parabola or a power-law function, both of which have been used by the Fermi Collaboration to build its source catalogues. To see how the neutrino upper limits and photon energetics compare, the gamma-ray spectral energy distributions (SEDs) of all sources have been produced using the SED builder of the ASI Science Data Centre (ASDC) [51] adding, if needed, VHE data taken from the literature, building a hybrid photon-neutrino SED [52]. The limits for different spectral indices, from -3 to -1, are extrapolated from the limits obtained in the E^{-2} energy spectra using the corresponding acceptance curve. Figure 14 shows the value of the neutrino flux limits for the five brightest sources as a function of the spectral indices. The range in energy for each limit corresponds to the 5-95% range of the energy distribution for a given spectra.

Figure 15 shows the hybrid SED for the lowest p-value source 3C279. The shaded yellow area represents an extrapolation of the flux during the studied flares from the average flux observed by Fermi. The lower bound is computed from the average flux during the 2008-2012 period, while the upper bound is simply the renormalised flux according to the maximum flux measured in the light curve. With this simple criteria of the energy budget, the limit set by ANTARES for the blazar 3C279 is of the same order of magnitude as the electromagnetic flux measurements during the flares. It reinforces the need to search for a neutrino signal during the outburst periods when the gamma-ray flux and the accompanying neutrino flux are much higher. Therefore, with more data, ANTARES should be able to significantly constrain a 100% hadronic origin of the high-energy gamma-ray emission. Fermi has reported some very intense outburst periods of 3C279 between mid 2013 and end of 2014 [55, 56], periods not considered in this paper.

Figure 16 shows the hybrid SEDs for the four additional bright blazars. These sources, classified as FSRQs, have their gamma-ray flux suppressed at high energy. Only the brightest FSRQ objects are detected at TeV energies. On the contrary, BL Lac objects have high-energy spectral components, favoured for TeV gamma-ray detection, but are fainter than FSRQs. Both FSRQs [57, 58] and BL Lac objects [59] have been argued to be potential sources of neutrinos. This comparison between the gamma-ray flux and the neutrino flux limit provides an indication as to how to build an optimised source list for future searches with ANTARES and its successor KM3NeT [60].

7 Summary

This paper discusses the extended time-dependent search for cosmic neutrinos using the data taken with the full ANTARES detector between 2008 and 2012. For variable sources, time-

dependent searches are significantly more sensitive than steady point-source searches thanks to the large reduction of the atmospheric background over short time scales. These searches have been applied to 41 very bright and variable Fermi LAT blazars and seven TeV flares reported by H.E.S.S, VERITAS or MAGIC telescopes. The most significant correlation was found with a GeV flare of the blazar 3C279 for which one neutrino event was detected in time/spatial coincidence with the gamma-ray emission. However, this event has a post-trial probability of 67%, and is thus compatible with background fluctuations. Upper limits were obtained on the neutrino fluence for the selected sources and compared with the high-energy component of the spectral energy distributions computed with GeV-TeV gamma-ray observations. These comparisons show that for the brighter blazars, the neutrino flux limits are of the same order of magnitude as the high-energy gamma-ray fluxes. With additional data from ANTARES and with the order of magnitude sensitivity improvement expected from the next generation neutrino telescope, KM3NeT, the prospects for future searches for neutrino emission from flaring blazars are very promising.

Acknowledgments

References

[1] J.K. Becker 2008, Phys. Rep., 458, 173.

[2] S.D. Bloom, A.P. Marscher, 1996, ApJ, 461, 657; L. Maraschi, G. Ghisellini, A. Celotti 1992, ApJL, 397, L5; C.D. Dermer, R. Schlickeiser, 1993, ApJ, 416, 458; M. Sikora, M.C. Begelman, M.J. Rees, 1994, ApJ, 421, 153.

[3] T.K. Gaisser, F. Halzen, T. Stanev, Phys. Rep. 258 (1995) 173.

[4] J.G. Learned, K. Mannheim, Ann. Rev. Nucl. Part. Sci. 50 (2000) 679.

[5] C.M. Urry, P. Padovani, 1995, PASP, 107, 803.

[6] F. Halzen, D. Hooper, Rep. Prog. Phys. 65 (2002) 1025.

[7] K. Mannheim, A&A, 269, 67, 1993.

[8] M. Böttcher, Astrophys. Space Sci. 309 (2007) 95.

[9] K. Mannheim, P.L. Biermann, 1992, A&A,253,L21.

[10] M. Böttcher, A. Reimer, K. Sweeney, A. Prakash, 2013, apJ, 768,54.

[11] M. Reynoso, G.E. Romero, M.C. Medina, A&A 545, (2012).

[12] A. Atoyan, C. Dermer, New Astron. Rev. 48(5) (2004) 381.

[13] A. Neronov, M. Ribordy, 2009, Phys.Rev., D80, 083008.

[14] A. Mücke, R.J. Protheroe, Proc. 27th Int. Cosmic Ray conf, arXiv:0105543.

[15] A. Mücke, R.J. Protheroe, Astropart. Phys. 15 (2011) 121.

[16] A.A. Abdo *et al.* 2010, ApJ, 715, 429.

[17] M. Ageron *et al.*, Nucl. Instrum. Meth. A 656 (2011) 11-38.

[18] J.A. Aguilar *et al.*, Phys. Lett. B 696 (2011) 16-22.

[19] S. Adrián-Martínez *et al.*, The Astrophysical Journal 760:53(2012).

[20] S. Adrián-Martínez *et al.* A&A Lett. 576 (2015) L8.

[21] S. Adrián-Martínez *et al.* Journal of High Energy Astrophysics 3-4(2014) 9-17.

[22] S. Adrián-Martínez *et al.*, *A&A* 559, A9 (2013)

[23] A.A. Abdo *et al.*. 2010, ApJ, 722, 520.

[24] M. Ackermann *et al.*, ApJ, 743 (2011) 171.

[25] T. Hovatta *et al.*, MNRAS arxiv:1401.0538.

[26] S. Adrian-Martinez *et al.*, Astropart. Phys. 36 (2012) 204-210.

[27] J. A. Aguilar *et al.*, Nucl. Instrum. Meth. A 555 (2005) 132-141.

[28] P. Amram *et al.*, Nucl. Instrum. Meth. A484 (2002) 369-383.

[29] S. Adrian-Martinez *et al.*, JINST 7 (2012) T08002.

[30] J. A. Aguilar *et al.*, Nucl. Instrum. Meth. A 570 (2007) 107-116.

[31] J. Brunner, VLVnT Workshop, Amsterdam 2003, ANTARES Simulation Tools, ed. E. de Wolf (Amsterdam: NIKHEF), 109; http://www.vlvnt.nl/proceedings.pdf.

[32] V.K. Agrawal, T.K. Gaisser, P. Lipari, T. Stanev, Phys. Rev. D53 (1996) 1314.

[33] Y. Becherini, A. Margiotta, M. Sioli, M. Spurio, 2006, Astropart. Phys., 25, 1.

[34] G. Carminati, A. Margiotta, M. Spurio, 2008, Comput. Phys. Commun., 179, 915.

[35] Margiotta. A., Nucl. Instrum. Methods A 725 (2012) 53.

[36] F. Schüssler, Proc. for the 33rd ICRC, Rio de Janeiro (2013) ID421.

[37] S. Adrián-Martínez *et al.*, Eur. Phys. J. C (2013) 73:2606.

[38] S. Adrián-Martínez *et al.*, in preparation.

[39] A. A. Abdo *et al.* 2013, ApJS, 208, 17.

[40] S. Ciprini *et al.*, 2011 Fermi Symposium proceedings - eConf C110509, arXiv:1111.6803. http://fermisky.blogspot.fr/

[41] http://fermi.gsfc.nasa.gov/cgi-bin/ssc/LAT/LATDataQuery.cgi.

[42] http://fermi.gsfc.nasa.gov/ssc/data/analysis/documentation/Cicerone/.

[43] J.D. Scargle, The Astrophysical Journal Supplement Series, 45, 1-71, 1981; http://trotsky.arc.nasa.gov/ jeffrey/.

[44] J.D. Scargle, Astrophys. J., 504, 1998, 405-418.

[45] J.D. Scargle *et al.*, Astrophys.J. 764 (2013) 167.

[46] J. Neyman, 1937, Phil. Trans. Royal Soc. London, Series A, 236, 333.

[47] M.G. Aartsen et al, submitted to ApJ, arXiv:1503.00598

[48] S.R. Kelner, F.A. Aharonian, V.V. Bugayov, 2006, Phys. Rev. D, 74, 034018.

[49] S.R. Kelner, F.A. Aharonian, 2008, Phys. Rev. D, 78, 034013.

[50] C. Tchernin, J.A. Aguilar, A. Neronov, T. Montaruli, Astron.Astrophys. 560 (2013) A67.

[51] http://tools.asdc.asi.it/SED/.

[52] P. Padovani, E. Resconi MNRAS, 443, 474 (2014).

[53] J. Aleksic et al, *A&A* 530, A4 (2011).

[54] J. Aleksic et al, *A&A* 567, A41 (2014).

[55] S. Buson, ATEL #5680 (2013).

[56] S. Ciprini, J. Becerra Gonzalez, ATEL #6036 (2014).

[57] K. Murase, Y. Inoue, C.D. Dermer, 2014, Phys. Rev. D, 90, 023007.

[58] C.D Dermer, K. Murase, Y. Inoue, 2014, submitted to J. High Energy Astrophys., arXiv:1406.2333.

[59] F. Tavecchio, G. Ghisellini, D. Guetta, 2014, arXiv:1407.0907.

[60] http://www.km3net.org
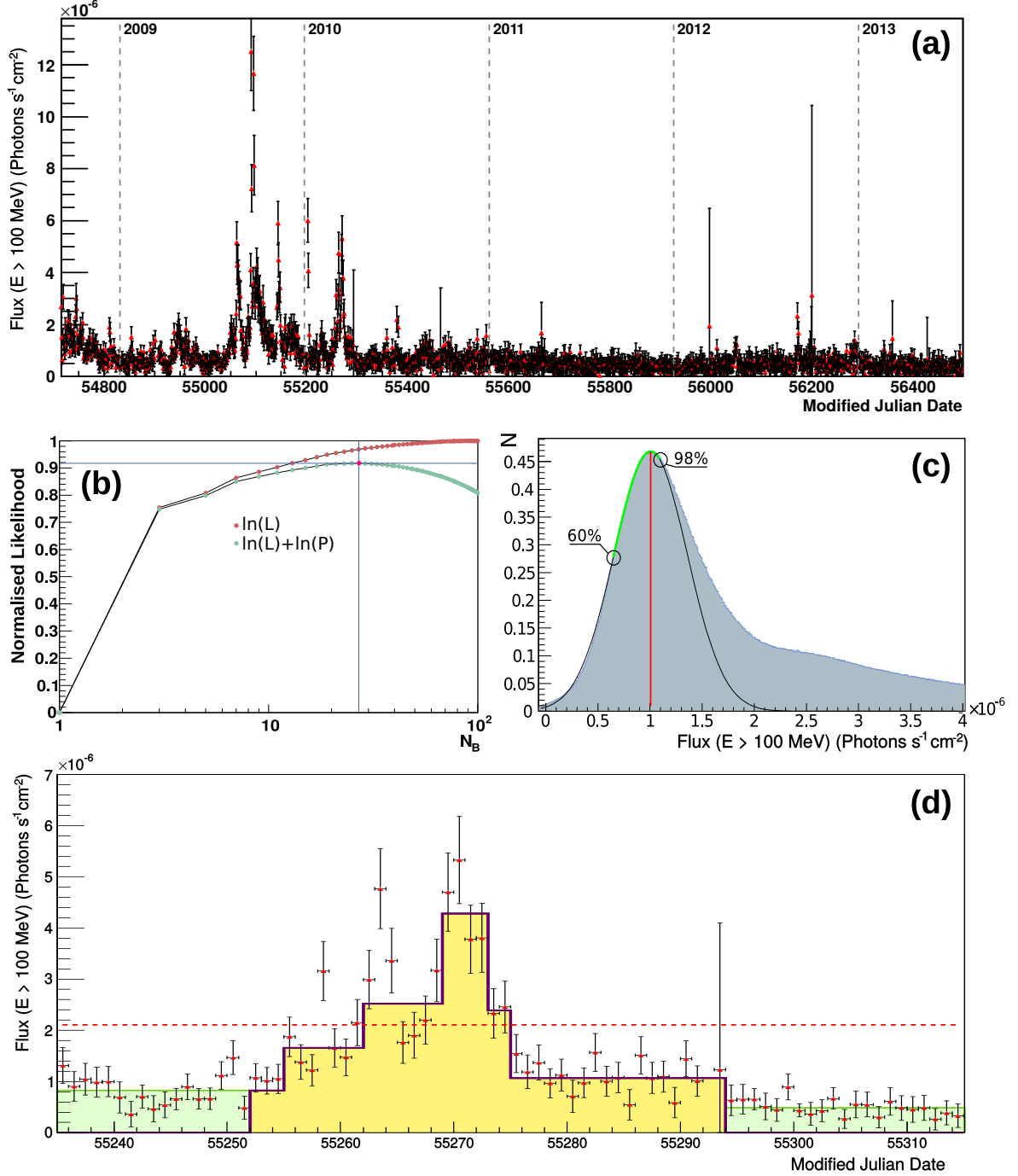
Figure 9. Illustration of the flare-selection concept using the maximum-likelihood block algorithm with the blazar 3C273. (a) Gamma-ray light curve using the 2008-2012 Fermi data with thershold of 100 MeV. (b) Evolution of the likelihood L (red dots) as a function of the number of added blocks (N_B). The green dots show the evolution after including the prior $\mathcal{P}$. The solid lines indicate the selected maximum. (c) Histogram of the flux convolved with a Gaussian distribution of the error on the flux. A Gaussian fit, shown by the black line, has been performed using data over the range (illustrated by the green line) between 60% (on the left-hand side) and 98% (on the right-hand side) of the maximum value. The value of the baseline is indicated by the red line. (d) Example of a selected flare of 3C273. Dots, the green and the yellow histograms display the raw data, the denoised light curve and the selected flare. The red dashed line corresponds to the 5σ threshold.
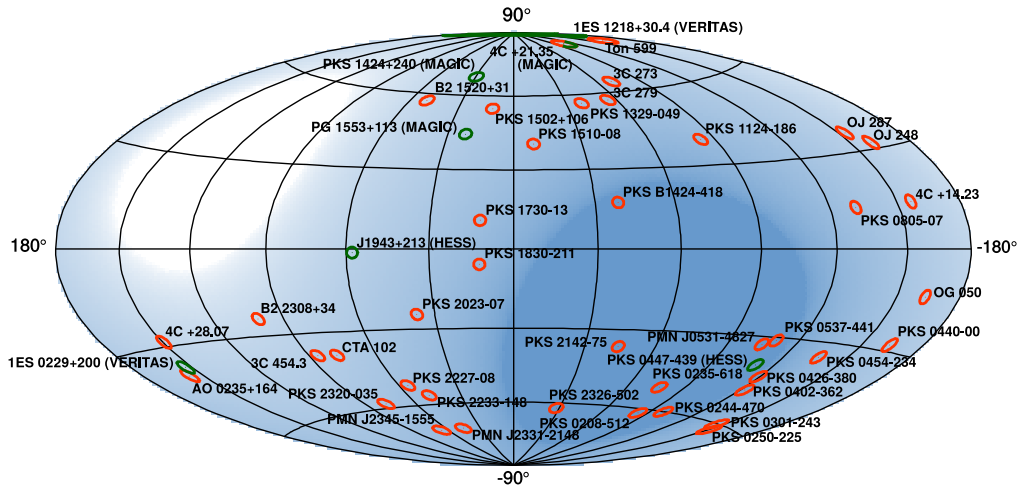
Figure 10. Skymap in galactic coordinates showing the position of the 41 selected Fermi blazars (red circles, see Section 4) and the seven TeV blazars (green circles, see Section 5) together with the ANTARES visibility (dark blue is maximal).
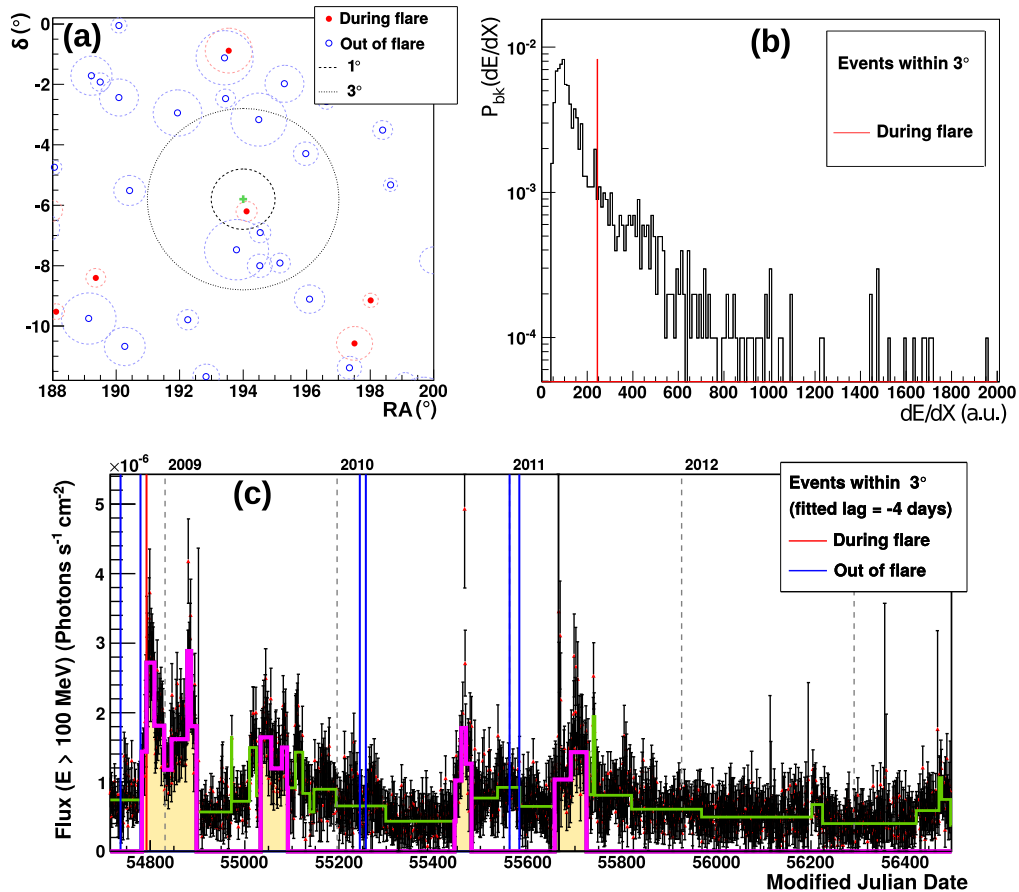
Figure 11. Results for the blazar 3C279. (a) Event map around the direction of 3C279 indicated by the green cross. The full red (hollow blue) dots indicate the events (not) in time coincidence with the selected flares. The size of the circle around the dots is proportional to the estimated angular uncertainty for each event. (b) Distribution of the energy estimator dE/dX in a ±10° declination band around the source direction. The red line displays the value of the event in coincidence with the flare in a 1° cone around the source direction. (c) Gamma-ray light curve (red dots) with the error bars (black) measured by the LAT instrument above 100 MeV. The green and purple histograms show the denoised light curve and the selected flare periods respectively. The red and blue lines display the times of the ANTARES events associated with the source during a flaring state and other events in a 3° box around the source position, respectively.
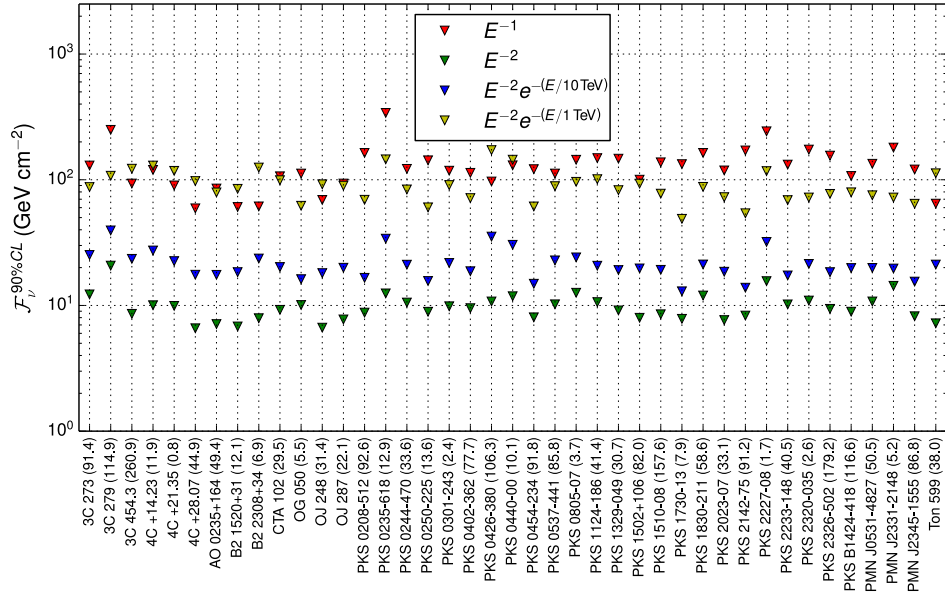
Figure 12. Upper limits on the neutrino fluence for the 41 studied Fermi blazars in the case of E^{-2} (green), $E^{-2} \exp(-E/10 \text{ TeV})$ (blue), $E^{-2} \exp(-E/1 \text{ TeV})$ (yellow) and E^{-1} (red) neutrino energy spectra. The number in parenthesis after the name of the source in the x-axis indicates the total effective flare duration Δt during the studied period.
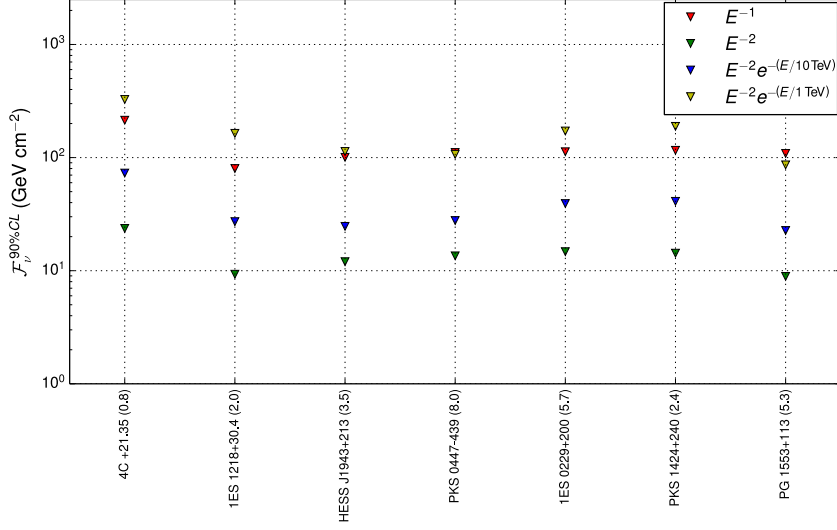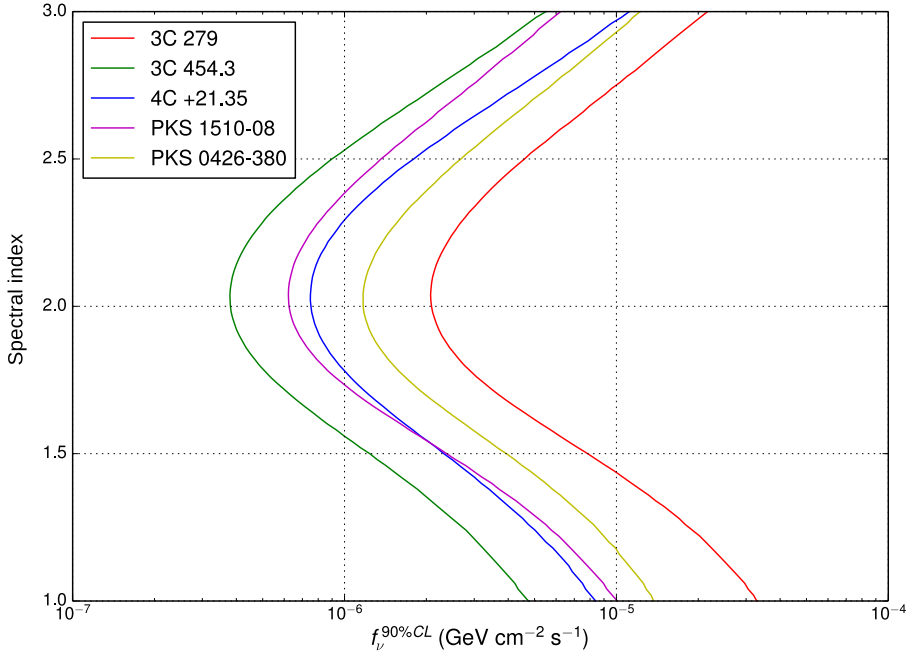
Figure 13. Upper-limits on the neutrino fluence for the seven studied TeV blazars in the case of E^{-2} (green), $E^{-2}\exp(-E/10\ \mathrm{TeV})$ (blue), $E^{-2}\exp(-E/1\ \mathrm{TeV})$ (yellow) and E^{-1} (red) neutrino energy spectra. The number in parenthesis after the name of the source in the x-axis indicates the total effective flare duration Δt during the studied period.

Figure 14. Extrapolation of the neutrino upper limit energy fluxes (integrated in the 5-95% energy range) from E^{-2} to other spectral indices for the five brightest Fermi blazars.
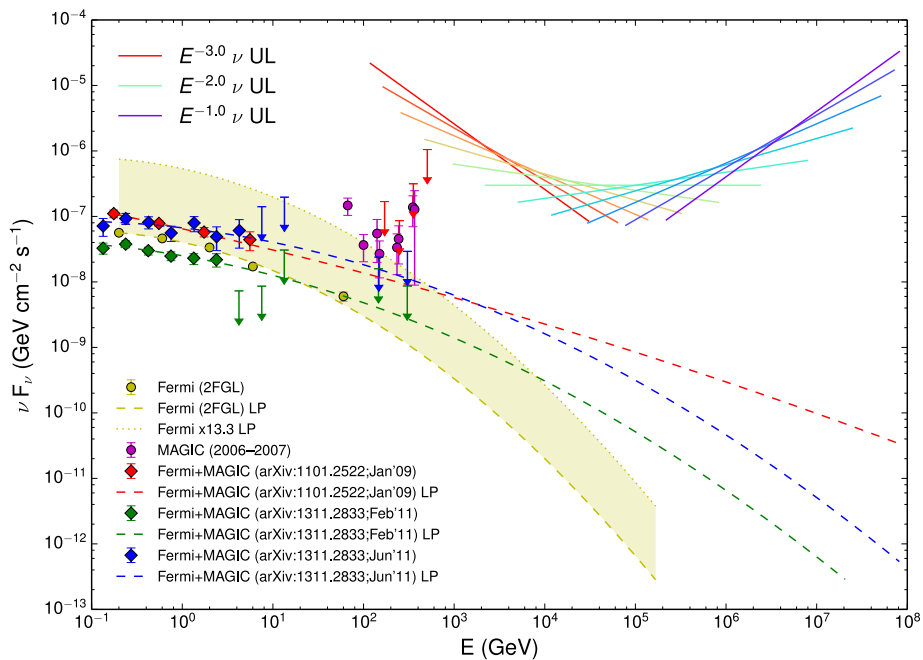
Figure 15. Gamma-ray SED of 3C279, observed by Fermi/LAT and MAGIC in January 2009 (red dots), January 2011 (green dots) and June 2011 (blue dots) [53, 54]. The yellow/green dots are the average flux with 2008-2010 data (2FGL). The observed data points are corrected for absorption by the extragalactic background light assuming z = 0.536. The dashed lines represents the fits performed on Fermi data using a log-parabola (LP) function. The shaded yellow area represents an extrapolation of the flux during the studied flares from the average flux observed by Fermi. The lower bound is computed from the average flux during 2008-2012 period, while the upper bound is the maximum flux measured in the light curve (x13.3 the average flux). Finally, the coloured solid lines indicates the neutrino upper limits for different spectral indices (from E^{-3} in red to E^{-1} in blue).
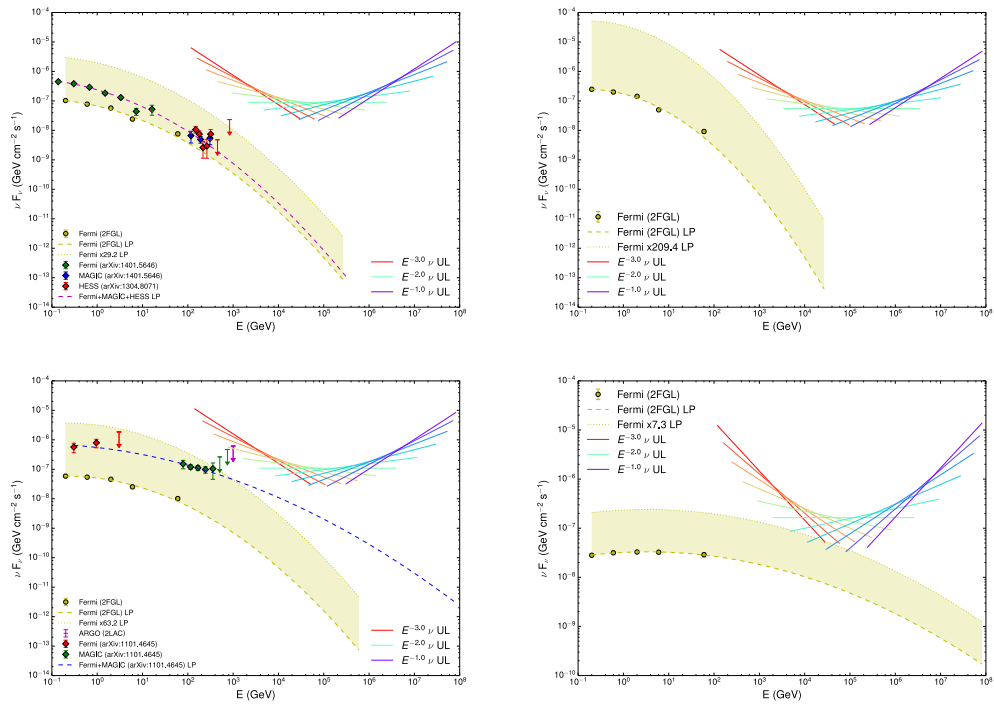
Figure 16. Hybrid SED of the four additional bright Fermi blazars PKS1510-089, 3C454.3, 4C21+35 and PKS0426. Points and lines are as described in the caption to Figure 15.